Acta Oceanol. Sin., 2020, Vol. 39, No. 7, P. 146–164
https://doi.org/10.1007/s13131-020-1619-8
http://www.hyxb.org.cn
E-mail: hyxbe@263.net

Demonstration of the refined three-dimensional structure of mesoscale eddies and computational error estimates via Lagrangian analysis

Heqing Yin[1], Haijin Dai[1]*, Weimin Zhang[1, 2], Xueyan Zhang[1], Pinqiang Wang[1]

[1] College of Meteorology and Oceanography, National University of Defense Technology, Changsha 410073, China

[2] Laboratory of Software Engineering for Complex Systems, Changsha 410073, China

Received 28 June 2019; accepted 11 September 2019

Abstract

In previous studies, Lagrangian analyses were used to assess large-scale ocean circulation, and the Lagrangian coherent structure could also reveal the evolution of the two-dimensional structure of the mesoscale eddies. However, few studies have demonstrated the three-dimensional structure of the mesoscale eddies via Lagrangian analysis. Compared with previous studies, which investigated the eddy structure via a Eulerian view, we used a Lagrangian view to provide a different perspective to study the eddy structure. An idealized cyclonic mesoscale eddy is built up over a seamount, and it presents downwelling inside the eddy and upwelling alongside the eddy formed within a closed circulation system. This structure is difficult to display via a Eulerian analysis. However, the trajectories of particles can well demonstrate the full cycle: the fluid sank and rotated inside the eddies, converged to the upwelling zone of the bottom layer and returned to the surface through upwelling. We also applied a Lagrangian analysis to a realistic simulation. As a significant phenomenon in the South China Sea, the dipole structure of the anticyclonic eddy (AE)/cyclonic eddy (CE) pair off of central Vietnam has been well studied but mainly at the sea surface. With a Lagrangian analysis, we illustrate the three-dimensional structure of the eddy pair: the fluid sank (rose) and rotated inside the AE (CE). More importantly, the trajectories of the particles suggested that there was no fluid exchange between the two eddies since the strong boundary jet separates them from each other. All the conclusions above have been verified and are supported by the computational error estimate. With a selected time step and integral period, the computational errors always present small values, although they increase with strong divergent and vertical diffusive flow.

Key words: mesoscale eddy, Lagrangian analysis, three-dimensional structure

Citation: Yin Heqing, Dai Haijin, Zhang Weimin, Zhang Xueyan, Wang Pinqiang. 2020. Demonstration of the refined three-dimensional structure of mesoscale eddies and computational error estimates via Lagrangian analysis. Acta Oceanologica Sinica, 39(7): 146–164, doi: 10.1007/s13131-020-1619-8

1 Introduction

Oceans exhibit a huge range of dynamical motions, large scale motions (>300 km), mesoscale motions (50–300 km), submesoscale motions (1–50 km) and small scale motions (<1 km) (McWilliams, 2016; Torres et al., 2018; Zhang et al., 2019). In slow-varying seawater, tracers (i.e., salt, heat, dissolved oxygen) carried by the fluid particles are used as seawater motion indicators. From a microscopic view, a particle is considered as a collection of a huge amount of molecules. Thus, velocity of the particle is defined as the mass weighted mean of the velocities of the individual molecules. When a great amount of fluid particles are integrated with three-dimensional (3D), time-evolving velocity fields, the trajectories of the particles depict the structure of the fluid field, which is the basis of the Lagrangian analysis.

Previous studies suggested that Lagrangian analysis was able to capture the primary structures of large-scale circulations both in the atmosphere (Kjellsson and Döös, 2012) and the ocean (Döös et al., 2008). However, the Hadley Cell (Deacon Cell) is a slow-varying and quasi-phase-locked phenomenon in the atmosphere (ocean) with a spatial scale of thousands of kilometers and kilometers in the horizontal and vertical directions, respectively. We sought to determine how the Lagrangian analysis performs for a smaller scale phenomenon with a varying velocity both in spatial and temporal dimensions. The typical phenomenon that comes to mind is the mesoscale eddy. As one of the most important mesoscale ocean phenomena, eddies have diameters of approximately 5–120 km and orbital velocities of 0.5–0.7 m/s (Johannessen et al., 1987; Adams et al., 2017). Strong mesoscale eddies can extend to several hundreds of meters in the vertical direction. Lin et al. (2018) traced a considerable number of tracers in a mesoscale eddy using a Lagrangian analysis, although they did not report the structure of the mesoscale eddy. In this study, the structure of the mesoscale eddy becomes our first priority to concern about.

To test how the Lagrangian analysis performs in demonstrating the 3D structure of the mesoscale eddy. We firstly build up an idealized eddy, which has a clearer and simpler 3D structure, compared with the real eddies in the ocean. In the second step, we try to apply the Lagrangian analysis to a realistic mesoscale

Foundation item: The National Key R &D Program of China under contract Nos 2018YFC1406202 and 2018YFC1406206; the National University of Defense Technology under contract No. ZK18-03-29.
*Corresponding author, E-mail: hj_dai@nudt.edu.cn

eddy, which is from the results of numerical simulation. As a robust phenomenon in the South China Sea (SCS), a dipole structure of anticyclonic eddy - cyclonic eddy (AE/CE) pair appears off the central Vietnam (Wang et al., 2006; Chu et al., 2014). The eddy generation mechanism is still debatable between three viewpoints. One suggests that the eddy pair is generated by the boundary jet, which is induced by the summer monsoon (Kuo et al., 2000; Xie et al., 2003; Wang et al., 2006). Wang et al. (2006) suggested the jet contains strong baroclinic instability. The dipole structure of wind stress curl (wind-driven) and the continental slope (potential vorticity conservation) are considered as the other two eddy generation mechanisms (Fang et al., 2002), although Fang et al. (2002) suggested the wind stress curl should be the dominant reason. The AE/CE pair usually is generated in June, reached its maximum intensity in August or September and disappeared in October. Eulerian analyses usually focus on the current structure at the surface. However, the Lagrangian analysis can well demonstrate the 3D structure of the eddy pair.

On the other hand, previous studies have usually neglected to provide computational error estimates with their experimental settings (i.e., time step, integration period). However, the computational error may be as large as hundreds of kilometers, which is even larger than the diameter of the mesoscale eddy. In this study, assume approximately constant mesoscale eddies in the idealized simulation, while employ the time-varying current in the realistic simulation; we demonstrated the structure of the mesoscale eddies using a Lagrangian analysis. We also provide estimates of the computational error obtained using different experimental settings to improve the reliability of our results.

This paper is arranged as follows. In Section 2, we introduce the Lagrangian calculation tool. In Section 3, we analyze the ideal eddy as an application of this tool. In Section 4, we analyze the AE/CE pair as an application of this tool. In Section 5, we provide a summary and identify future research topics.

2 Introduction to the Lagrangian analysis method

The Lagrangian calculation tool implemented here (van Sebille et al., 2018) begins with an analysis the output from general circulation models (i.e., general ocean circulation model or general atmospheric circulation model) or other velocity data. The velocity would be interpolated into the coordinate redefined for further analysis. Usually, the interpolation methods in the horizontal directions (i.e., bilinear interpolation) are different from that in the vertical direction (i.e., tension spline curve). The distance that the particle undergoes is estimated with implicit, explicit or semi-implicit iterative methods (i.e., 4th order Runge-Kutta scheme (RK4)) both in the spatial and temporal dimensions. Together with the initial location and the movement vector, the new transient location of the particle is estimated. The Lagrangian trajectory of the particle is depicted with a considerable number of transient locations.

When the actual trajectory of a particle is divided into n parts, each part of its trajectory can be viewed as the journey of the particle during a short period. Considering that the particle has a velocity of (u_n,v_n,w_n) and undergoes a period of δt from (u_n,v_n,w_n) to $(u_{n+1},v_{n+1},w_{n+1})$, there is

$$x_{n+1} = x_n + u_n\delta t, \tag{1}$$

$$y_{n+1} = y_n + v_n\delta t, \tag{2}$$

$$z_{n+1} = z_n + w_n\delta t, \tag{3}$$

Realistically, the current varies in different locations and its trajectory during a given period may be a curve. Furthermore, we considered that each particle has the same velocity during one time step in the model; thus, a computational error (Fig. 1) was introduced using the Lagrangian calculation. Fortunately, as long as we employ a small time step and use the Lagrangian calculation within a reasonable period, we can maintain the computational error within an acceptable range. When we demonstrate the 3D structure of the eddy using Lagrangian calculations in the following sections, we always maintained a sufficiently short time step and integral period to maintain acceptable computational errors.

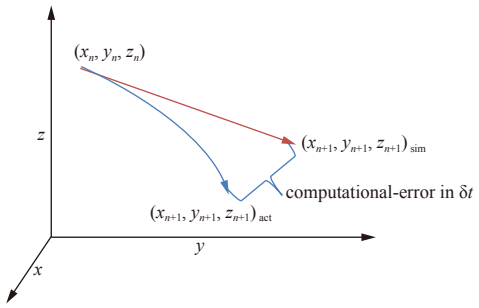

Fig. 1. Figure of the trajectory during the $(n+1)$th timestep: $(\,)_{\text{act}}$ represents the particle's actual location after the $(n+1)$th time step, while $(\,)_{\text{sim}}$ represents the particle's location calculated by the Lagrangian calculation tool.

The Lagrangian calculation tool used in this study is the Lagrangian TRANSport model (LTRANS), which is an off-line particle-tracking model that runs with the stored predictions of a three-dimensional (3D) hydrodynamic model, i.e., Regional Oceanic Modelling System (ROMS, Shchepetkin and McWilliams, 2005; Lemarié et al., 2012). LTRANS can simulate passive particles or particles with sinking or floating behaviors, i.e., sediment, oil droplets or planktonic organisms (we used the passive particle option in this study). LTRANS is designed to track the trajectories of particles in three dimensions.

In this study, ROMS was employed to simulate the idealized and realistic mesoscale eddies. However, the method of producing these eddies is not a focus of this study. As a result, additional details on the production of the idealized mesoscale eddy with ROMS is introduced in Appendix A. The Eulerian analysis of the idealized mesoscale eddy is also described in Appendix A. Similarly, more detail about how we reproduce the AE/CE eddy pair off the central Vietnam with ROMS-4DVAR is introduced in Appendix B. Eulerian analysis of the AE/CE eddy pair is also presented in Appendix B.

3 Demonstrate the refined structure of cyclonic mesoscale eddies over a seamount via a Lagrangian analysis

In order to apply a Lagrangian analysis to the mesoscale eddy, we first employed an idealized mesoscale eddy, whose structure is clearer and simpler than the realistic oceanic mesoscale eddy. The idealized mesoscale eddy was produced by the generation mechanism of baroclinic instability, we also employed a seamount to ensure that this eddy did not move.

The primary mesoscale eddy was located in the middle of this domain, where the seamount is set beneath. The current moved cyclonically (Fig. 2a, vector), which indicates a positive vorticity (Fig. 2a, shading). To better depict the outline of the mesoscale

eddy, the eddy boundary is defined as follows (Okubo, 1970; Weissa, 1991):

$$W = s_{\mathrm{sh}}^2 + s_{\mathrm{st}}^2 - \zeta^2, \tag{4}$$

$$\text{eddy boundary} = -0.6 \times \mathrm{std}\,(W)\,, \tag{5}$$

where s_{sh} and s_{st} are the shear and strain deformation, respectively, ζ is the vertical component of vorticity, and std(W) is the standard deviation of W.

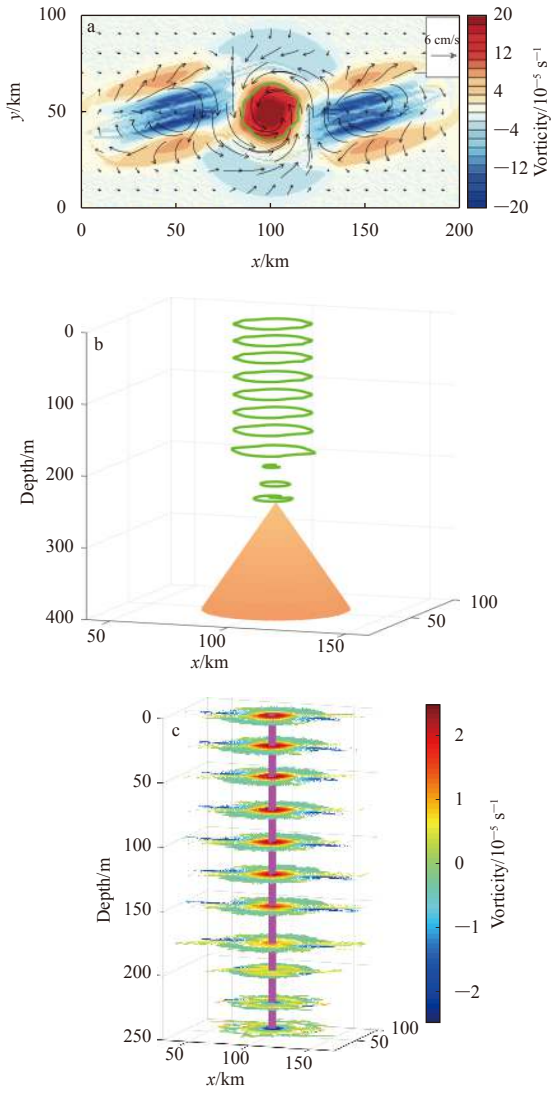

Fig. 2. The distributions of the surface current and vertical vorticity (a); the eddy boundary (green contours) at different layers (b); and the vertical vorticities in different layers (c).

Based on the eddy boundary definition, the diameter of the primary eddy is approximately 29 km at the surface (Fig. 2a, green line). The eddy boundary definition is applied to the lower layers, and the outline of the mesoscale eddy is depicted (Fig. 2b, green line). The eddy was nearly a cylinder above 180 m and then shrank at greater depths, and its diameter was only 3 km at a depth of 210 m before it widened to 13 km at a depth of 245 m. The distribution of the vorticity suggested that the current moved cyclonically above 180 m and moved anticyclonically in lower layers (Fig. 2c). The current moved faster at the surface and slower in deeper layers; and the distribution of the current speed was similar in each layer (not given).

3.1 *Experiment settings for Lagrangian analysis of idealized mesoscale eddy*

Using the Lagrangian analysis, we first studied the two-dimensional (2D) structure. By assuming that particles were always floating in the same layer, we neglected vertical motion for the sake of simplicity. As the computational error increased with faster flow, the surface and bottom layers were chosen for demonstration. Since the velocity distribution was similar in the upper layers, we felt that the surface layer was a good choice. In Exp1 and Exp2, the time steps were set to 60 s. We also chose 5 additional time steps ranging from 1 to 600 s to test the sensitivity of the computational error. At the sea surface, we released the particles outside the mesoscale eddy (Exp1 and Assum Exp1). At the bottom layer, we released the particles near the seamount (Exp2 and Assum Exp2). Assum Exp* indicates the sensitivity experiments of Exp*. More details are shown in Table 1.

In the 3D structure demonstration, we added vertical motion. To assess the sensitivity of the computational error, we used 6 time steps ranging from 1 to 600 s as in the 2D structure experiment. To demonstrate the 3D structure of the mesoscale eddy or visualize the upwelling and downwelling, we released the particles at the surface eddy boundary (Exp3 and Assum Exp3) and in the bottom layer (Exp4, Assum Exp4, Exp5 and Assum Exp5) and chose the particles that formed the mesoscale eddy for analysis. More details are shown in Table 1.

As the experiment used in this study is idealized, we assumed that the trajectory calculated with a time step of 1 s approximates the "real trajectory", which is much smaller than the actual time step in the ROMS model (15 s) and was used to estimate the computational error obtained with different time step selections.

Table 1. Experimental settings for the Lagrangian analysis applied to the idealized mesoscale eddy

Name	Displayed dimensions	Time step/s	Location where particles released	Integration period/h	Released particle number
Exp1	2 (x–y)	60	surface eddy boundary	800	1 000
Exp2	2 (x–y)	60	the bottom of the seamount	800	1 000
Exp3	3 (x–y–z)	30	surface eddy boundary	800	5 000
Exp4	3 (x–y–z)	30	upwelling zone at the bottom layer	800	10 000
Exp5	3 (x–y–z)	30	the bottom of the seamount	800	10 000
Assum Exp1	2 (x–y)	1, 5, 30, 300, 600	surface eddy boundary	800	100×5
Assum Exp2	2 (x–y)	1, 5, 30, 300, 600	the bottom of the seamount	800	100×5
Assum Exp3	3 (x–y–z)	1, 5, 60, 300, 600	surface eddy boundary	800	100×5
Assum Exp4	3 (x–y–z)	1, 5, 60, 300, 600	upwelling zone in the bottom layer	800	100×5
Assum Exp5	3 (x–y–z)	1, 5, 60, 300, 600	the bottom of the seamount	800	100×5

3.2 *Two-dimensional structure of the eddy*

We released the particles at the boundary of the mesoscale eddy at the sea surface (Exp1), and the particles started to move close to the center of the eddy. Meanwhile, the particles rotated cyclonically (Fig. 3a). The particles arrived at the center of the eddy in 400 h. We performed the same experiment in the lower layers of the eddy; as long as the vorticity was positive, the trajectories of the particles shared similar velocity distributions.

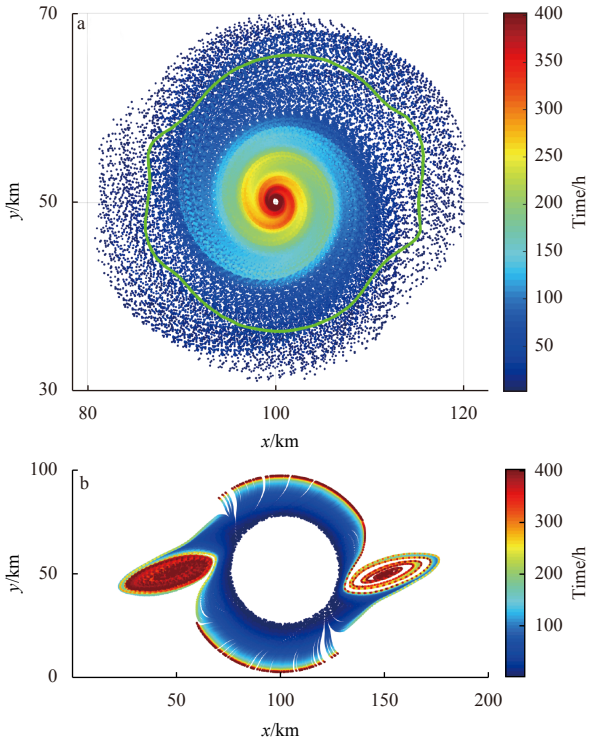

Fig. 3. Horizontal movements of the particles (dots) and eddy boundary (green line) in the surface and bottom layers are shown in a and b, respectively.

We released the particles at the bottom of the seamount (Fig. 3b, Exp2), and they moved against the seamount and remained where upwelling eventually occurred. In the south-north direction, the particles moved in the direction of upwelling. In the east-west direction, however, when the particles reached the upwelling zone, they moved towards the center of the upwelling and rotated cyclonically based on the vorticity distribution. The particles remained nearly static after 250 h and 400 h in the south-north and east-west directions, respectively.

3.3 *Three-dimensional structure of the eddy*

The calculation of 3D flow became more complex, and the computational error grew to reach unexpected values. To describe the eddy structure, we should explain two important features. First, we should describe how the particles moved in the mesoscale eddy. The Eulerian view (Appendix A) suggested that downwelling occurred inside the primary mesoscale eddy. We released the particles at the sea surface and outside the mesoscale eddy (Exp3). Over time, the particles sunk down to lower layers due to downwelling (Fig. 4a), and the color distribution in the vertical direction suggested that the vertical velocity in the mesoscale eddy was relatively uniform. The particles also rotated cyclonically as they moved towards the center of the eddy and reached the central part in 400 h. When the particles reached the seamount, which was located outside the eddy, the particles sunk along the slope, reached the bottom layers, and moved upwards due to upwelling. We also released particles close to the boundary of the mesoscale eddy in lower layers, and most of these particles shared similar trajectories.

The particles released at the surface demonstrated the structure inside the mesoscale eddy. Next, we demonstrated the source of these particles as a second feature of the mesoscale eddy. We released the particles in the upwelling zone at the bottom layer (Exp4, Fig. 4b), and their trajectories were different with those released at the bottom of the seamount (Exp5, Fig. 4c). These trajectories suggested that the particles released in the upwelling zone could flow to the surface layer. A vertical view suggested that these particles moved upward to the surface via upwelling near the north-south boundary and in the center of the upwelling zone on the eastern and western sides of the seamount (Fig. 4d), where these particles eventually remained in the 2D experiment (Fig. 3b). Another issue we found is that the particles entered the eddy in different layers. The lower the layer in which the particles entered the eddy was, the shorter the period they needed. We released the particles in different layers, and some of them entered the mesoscale eddy while the rest remained outside the mesoscale eddy. However, the results suggested that only the particles released in the upwelling zone at the bottom layer could travel back to the surface layer.

The 3D structure of the mesoscale eddy was described as the rotation and then sinking of the water inside the eddy down to its lower layers. The water flowed out from the bottom of the eddy and along the slope of the seamount to reach the bottom layer. Because of strong convergence, the water outside the eddy was sucked into the eddy in its upper layers, and it was compensated by the water particles transported by upwelling from lower layers or by downwelling from upper layers (not shown). However, the source of the water in the surface layer could only be derived from the bottom layer and transported via upwelling surrounding the mesoscale eddy.

3.4 *Computational error estimate and discussion*

Sensitivity experiments, which are introduced in Table 1, were employed for estimating and discussing the computational error.

3.4.1 *Time step and integration period*

In the 2D experiments (Exp1, Assum Exp1, Exp2 and Assum Exp2), the computational errors generally increase with larger time steps. At the sea surface (Exp1 and Assum Exp1, Fig. 5a), the magnitude of the computational error always maintained at a small amplitude (no more than 0.045 km) in the convergent flow. However, the computational errors grow gradually in the bottom layer (Exp2 and Assum Exp2) since divergent flow occurs. The computational error grew as much as 6 km (Fig. 5b), which was 100 times greater than that at the sea surface. However, we found that when the time step was smaller than 60 s, the maximum computational error was no more than 1 km, which meant that the particles may have stayed in the same grid and shared the same physical features. In conclusion, we suggest that the time step in the Lagrangian analysis of 2D flow should be smaller than 60 s and that the trajectory should be calculated over a long time period (e.g., 500 h).

In the 3D experiments, the computational errors grew slowly in a convergent flow (Exp3 and Assum Exp3, Fig. 5c). When the particles moved in the eddy with an integration period of less

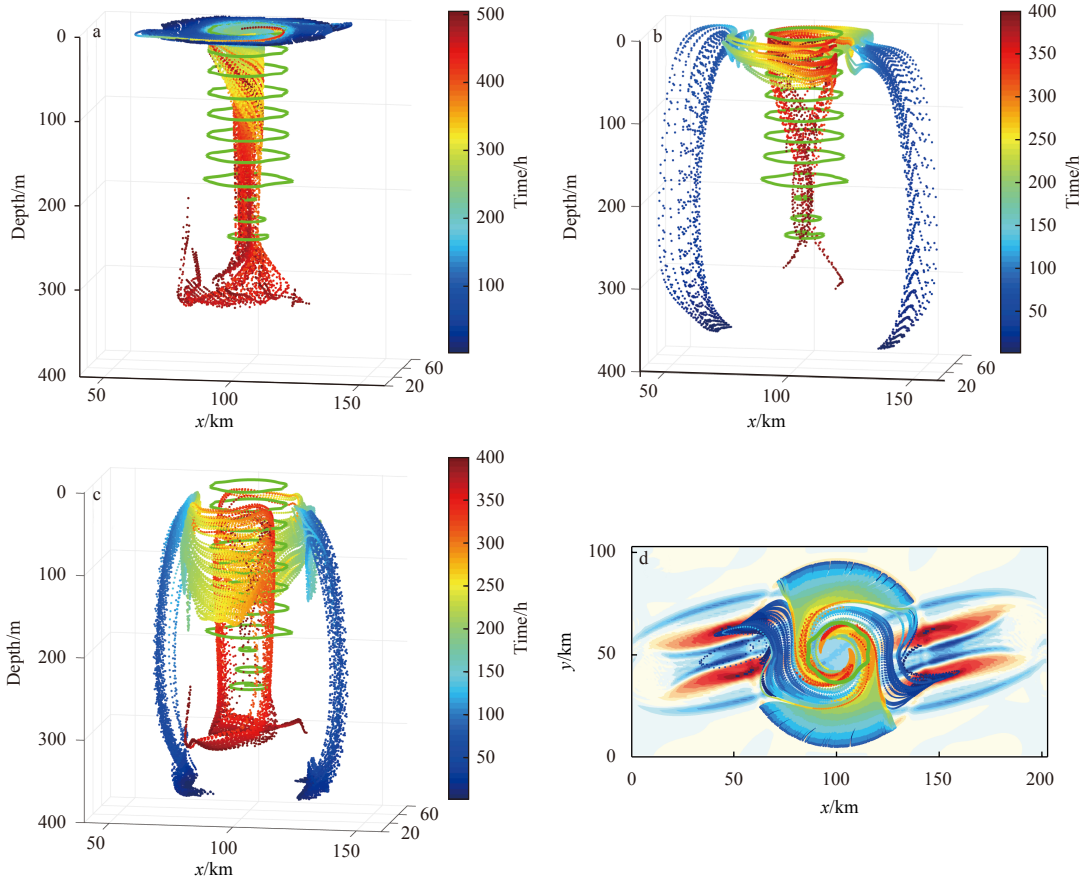

Fig. 4. Particles released outside the surface eddy boundary (Exp3) and their tracked trajectories (a) particles released in the upwelling zone at the bottom layer (Exp4) and their tracked trajectories (b), particles released at the bottom of the seamount (Exp5) and their tracked trajectories (c),and vertical view of b and the depth-averaged vertical velocity (shading, unit: 0.1 mm/s (d).

than 450 hours, the computational error was always maintained below 1 km. Outside the eddy (Exp4, Assum Exp4, Exp5 and Assum Exp5), however, the computational error increased up to 40 km (Fig. 5d) after 450 hours of integration. When the time step was smaller than 60 s, the computational error could be maintained at small values for a long period. In contrast, when the time step was longer than 300 s, the computational error grew significantly and could not be ignored in a short integration period.

We need to make a note here. The discussion above focused on the worst trajectory simulation. However, for most (85%) of the particles' trajectories, the computational error could always be maintained below 2 km over 800 h of integration when the time step is smaller than 60 s (not given). In summary, when the time step of the Lagrangian analysis is no more than 60 s, the simulations of most of the particles' trajectories are acceptable. If we only integrate the Lagrangian analysis for 450 h, nearly all the trajectories are acceptable.

3.4.2 *Current features*

The computational error is determined not only by the model setting (i.e., the time step and integration period) but also by the current features. In this study, we checked several current features, such as divergence, vorticity, vertical velocity shear and current speed. In general, the correlation coefficient between the current feature and the growth rate of the computation error increases (Fig. 6), as the time step gets larger (larger computational error). The growth rate of the computational error is equivalent to growth of the computational error during a short period, i.e., 1 hour. In the upwelling, the correlation coefficient between the divergence (Fig. 6a; vertical velocity shear, Fig. 6b; current speed, Fig. 6c) and the growth rate of the computational error is more than 0.2 (0.17, 0.07), which indicates that a faster current or flow with larger vertical shear and divergence may increase the computational error. On the other hand, the correlation coefficient between the vertical vorticity and the growth rate of the computational error (Fig. 6d) is nearly –0.08, which means that strong anticyclonic rotation may increase the computational error. In the downwelling, the correlation coefficient between the divergence (Fig. 6e; vertical velocity shear, Fig. 6f) and the growth rate of computational error is nearly 0.18 (0.27), which is consistent with the results in the upwelling. However, the correlation coefficient between the current speed and the growth rate of computational error (Fig. 6g) is –0.02, which is inconsistent with the result for the upwelling, and the relation is not significant. The correlation coefficient between the vertical vorticity and the growth rate of computational error (Fig. 6h) is only –0.14, which is much smaller than that in the upwelling. As a result, we conclude that the growth rate of computational error is determined by the divergence and vertical velocity shear, and it may also be influenced by the vertical vorticity. However, the current speed may not determine the growth rate of the computational error. (Note: Because the number of the samples is as large as 80 000, when the correlation coefficient is larger than 0.06, it should achieve significance based on the *t*-test.)

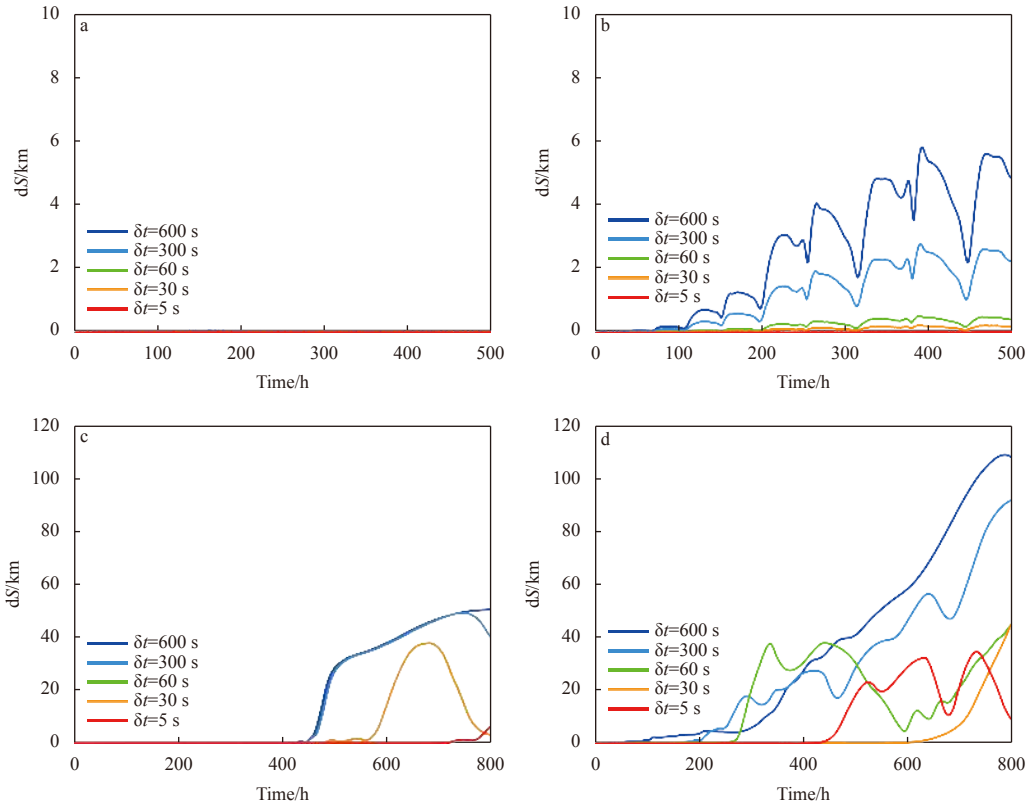

Fig. 5. Maximum computational error estimates obtained with different time steps when the particles moved in the surface (Exp1 and Assum Exp 1) and bottom layers (Exp 2 and Assum Exp 2) in the 2D experiments (a) and (b), and maximum computational error estimates obtained with different time steps when the particles moved in the downwelling (Exp 3 and Assum Exp 3) and upwelling (Exp 4, Assum Exp 4, Exp 5 and Assum Exp 5) in 3D experiments (c) and (d). The blue, cyan, green, orange, and red lines indicate the computational errors obtained using the time steps of 600 s, 300 s, 60 s, 30 s and 5 s, respectively.

4 Demonstrate the dipole structure of cyclonic and anticyclonic eddies near Vietnam with Lagrangian analysis

West part of SCS (4°–18°N, 106°–116°E) was simulated with the regional ocean model ROMS, which has a horizontal resolution of (1/20)°. An additional strong constraint 4D-Var (I4DVAR) scheme (Moore et al., 2011) is also implemented to perform the data assimilation with the satellite observations (sea surface temperature (SST), sea level anomaly (SLA)) and *in situ* T/S profile (Argo, Conductivity-Temperature-Depth recorder (CTD) and etc.). More details are presented in Appendix B.

The AE/CE pair located in the region of (8°–14°N, 109°–113°E) (Figs 9 a and b) is consistent with the observations through the whole September. Take the current distribution on September 13, 2013 as a typical example. The eddy boundary defined here is not OW, and we followed the definition by Dong et al. (2012) and Nencioli et al. (2010). The AE mainly occurred in the upper 350 m. Across the AE/CE pair (Fig. 7a, green line), there is eastward flow in the south (north) part of the CE (AE), while westward flow (Fig. 7c) appears in the north (south) part of the CE (AE), which indicated that the current rotated cyclonically (anticyclonically) in the CE (AE). As a result, downwelling (upwelling) appeared in the AE (CE), although the vertical motion is not totally horizontally uniform inside the eddies. Disturbed by the vertical flow, the isotherms (Fig. 7d, blue contour) sank (lifted) in the AE (CE). Although the AE is stronger than the CE and has a larger radius (Fig. 7a), the CE (Fig. 7b, blue line) extended to deeper layers than the AE (more details are shown in Appendix B).

4.1 *Lagrangian analysis experiment settings*

Following Section 4.1, we first studied the 2D structure of the AE/CE pair. The scenario can be viewed as we tracked the floating tracers (i.e., Argo, glider) in the same layer. Thus, we neglected vertical motion and released the particles at the upper layer (z=–28 m, where the vertical motion began to become significant in CE, $|w|>0.124$ mm/s) between the eddy center and eddy boundary both in the AE and CE (Exp6, current is considered as constant as that on September 13, 2013). In Exp6, the time step was set to 60 s. We also selected another 5 time steps ranging from 1 to 600 s to test the sensitivity of the computational error. The sensitivity experiments were named as Assum Exp6, which were corresponding to Exp6. More details are shown in Table 2.

In the 3D structure demonstration, we added vertical motion. To assess the sensitivity of the computational error, we used 6 time steps ranging from 1 to 600 s as in the 2D structure experiment. The particles are released in the whole layers both in the CE (Assum Exp7) and in the AE (Assum Exp8). However, to better reveal the realistic water motion inside the dipole eddy-pair, we applied the Lagrangian analysis to time-varying current field, which is from the realistic simulation results, to demonstrate the 3D structure of the mesoscale eddy. We released the particles at the same location as Exp6 (only in the AE, Exp7). We also released the particles at the lower layer of AE (z=–352 m, where it is the bottom of CE, Exp8) and selected the particles that formed the mesoscale eddy for analysis. In the Exp7 and Exp8, we released the particles on September 1, and the Lagragian analysis is integrated through the whole September, with the correspond-

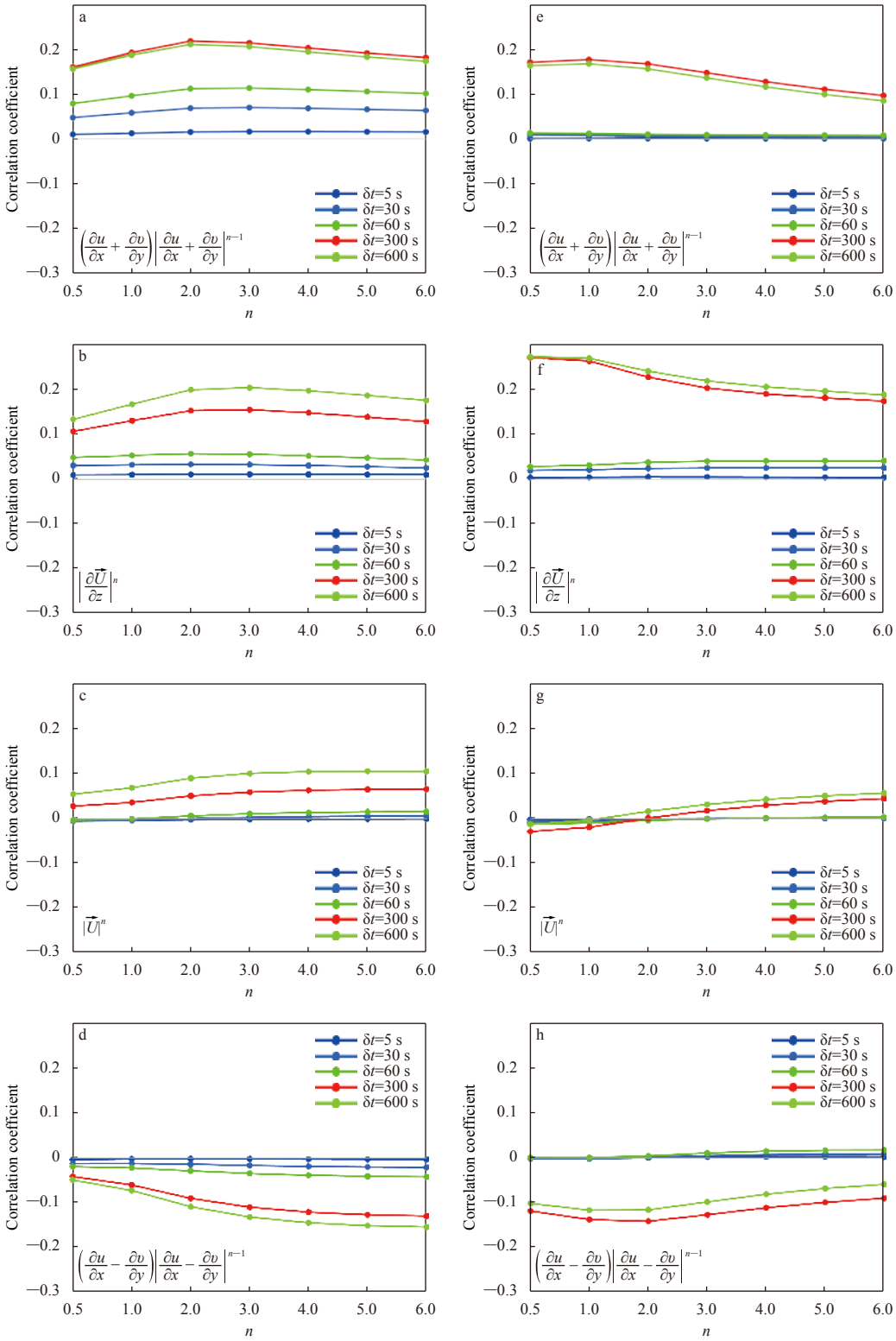

Fig. 6. Correlation coefficients between the growth rate of the computational error and the current features in the AE are estimated. Current features include the divergence $\left(\frac{\partial u}{\partial x}+\frac{\partial v}{\partial y}\right)$ (a), vertical shear $\left(\left|\frac{\partial \vec{V}}{\partial z}\right|=\left|\frac{\partial u}{\partial z}\vec{i}+\frac{\partial v}{\partial z}\vec{j}\right|\right)$ (b), current speed $\left(\left|\vec{V}\right|=\left|u\vec{i}+v\vec{j}\right|\right)$ (c), and vertical vorticity $\left(\frac{\partial v}{\partial x}-\frac{\partial u}{\partial y}\right)$ (d), and we also consider the nth power of the variable (n=0.5, 1, 2, 3, 4, 5, 6; however, we always kept the sign of the variable). e, f, g, h are same as a, b, c, d but are correlation coefficients in the CE. The blue, cyan, green, orange, and red lines indicate the correlation coefficient obtained using the time steps of 600, 300, 60, 30 and 5 s, respectively.

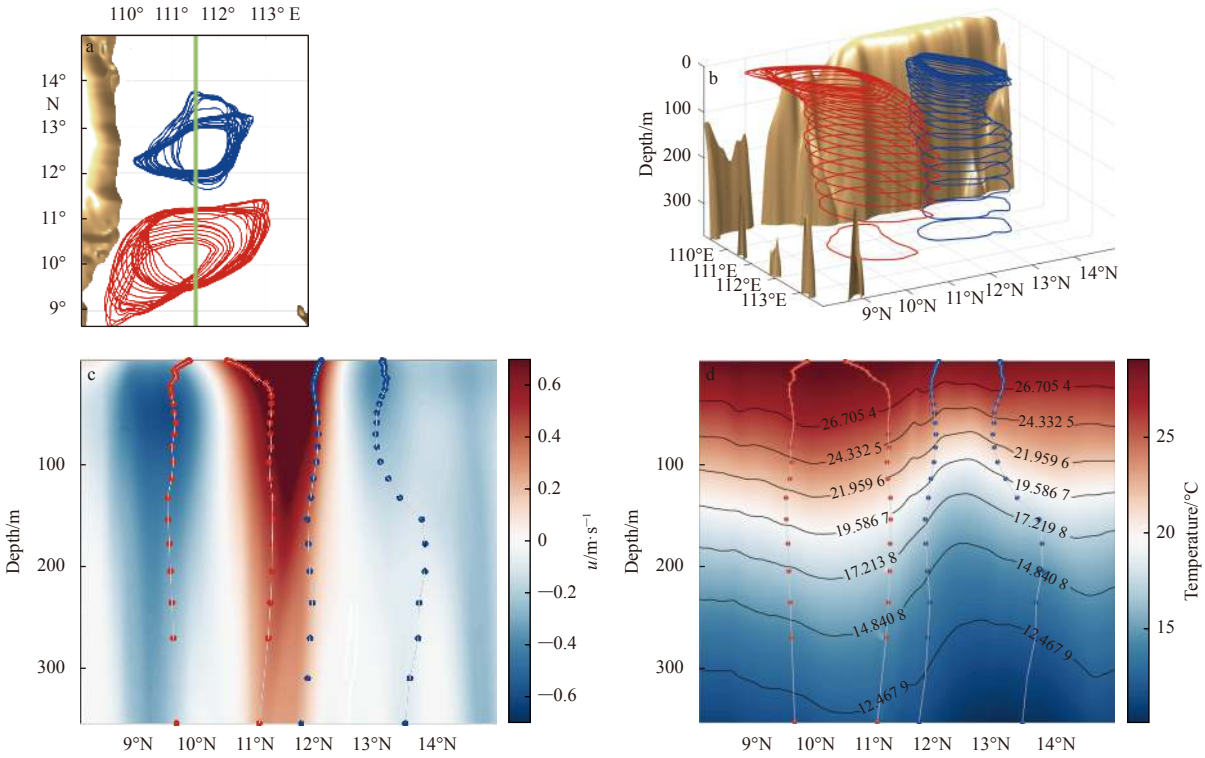

Fig. 7. Vertical view of the eddy boundary of AE (red line) and CE (blue line) in each layer (a), with a green line nearly across the centers of the two eddies; the 3D structure of the eddy boundary (b) (the orange shading indicates the topography); and the vertical profile of the velocity in the meridional direction and the temperature along the green line in a (c and d). The red and blue dot lines represent the eddy boundary in each layer. Selected isotherms are also presented as contours in d.

Table 2. Experiment settings for the Lagrangian analysis applied to the eddy pair simulation (Vietnam dipole)

Name	Displayed dimensions	Time step/s	Location where particles released	Integration period/h	Released particle number
Exp6	2 (*x*–*y*)	60	*z*=–28 m, AE, CE, in the middle between the eddy center and the eddy boundary	1 440	5 600×2
Exp7	3 (*x*–*y*–*z*)	30	same as Exp6, but only in AE	720	6 000
Exp8	3 (*x*–*y*–*z*)	30	*z*=–352 m, CE, in the middle between the eddy center and the eddy boundary	720	6 000
Assum Exp6	2 (*x*–*y*)	1, 5, 30, 300, 600	same as Exp6	1 440	600×5
Assum Exp7	3 (*x*–*y*–*z*)	1, 5, 30, 60, 300, 600	through the layer *z*=–28 to *z*=–352, in the middle between the eddy center and the eddy boundary, but only in CE	1 440	300×6
Assum Exp8	3 (*x*–*y*–*z*)	1, 5, 30, 60, 300, 600	same as Assum Exp7, but in AE	1 440	300×6

ing simulation.

4.2 *2D structure of the AE/CE pair*

In the upper layer (*z*= –28 m, Exp6, Figs 8a, b), we release the particles inside the AE and CE. Convergence occurs in the AE, and the particles move closer to the center of the AE after 1 440-hour integration (Fig. 8a), whereas divergence occurs in the CE, and the particles spread toward outside the CE, and reached as far as 200 km after 1 440-hour integration (Fig. 8b). Meanwhile, the particles rotated anticyclonically.

4.3 *3D structure of the AE/CE pair*

Based on the distribution of the flow, the particles motion was relatively simple in the AE/CE eddy pair. Particles were released in the upper layer of AE (Exp7, Figs 9a, b) and sank to lower layers gradually since there was mostly downwelling inside the AE. However, the particles were eventually located in different depths at the end of the experiment, which indicated that vertical motion is not horizontally uniform inside the AE. A typical particle can well demonstrate how the flow moved inside the AE, and we found that the particle sank from –28 m to –262 m (Fig. 9b) and rotated anticyclonically.

Similarly, particles were released in the lower layer of CE (Exp8, Figs 9c, d) and gradually moved upward to upper layers (Fig. 9c). The wavy distribution in the vertical direction suggested that the upwelling is not horizontally uniform inside the CE. We also employed one particle to demonstrate the structure of the flow inside the CE (Fig.9d). We found that the particle rose from –352 m to shallower than –52 m after 720 hours of integration, and it rotated anticyclonically. The results suggested that vertical motion is stronger in the AE than the CE, which is consistent with our earlier conclusion. On the other hand, we found that fluid exchange did not occur between the AE and CE. The

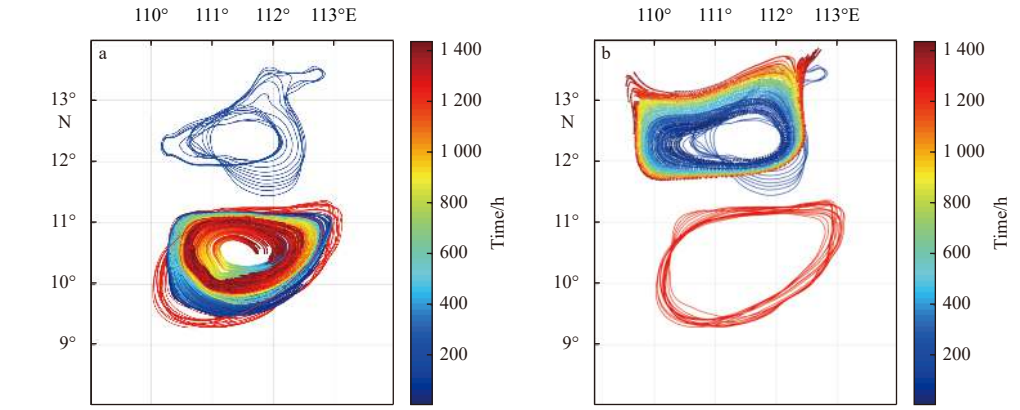

Fig. 8. Particles released at z=–28 m in Exp6; the trajectories of the particles in a AE and b CE are tracked by the dots, whose colors change with time. The eddy boundary in each layer of AE (red line) and CE (blue line) on September 13, 2013 are shown.

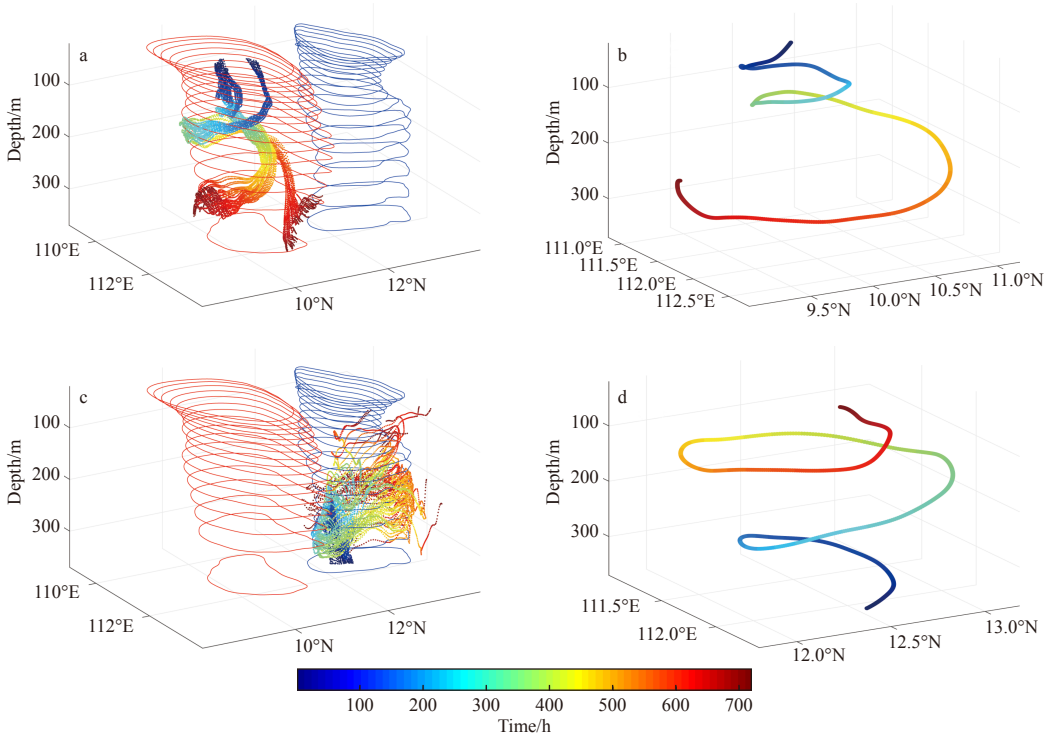

Fig. 9. Particles released at z=–28 m/–352 m inside AE/CE in Exp7/Exp8 (the trajectories of the particles are tracked by dots, and the color indicates the integration period)(a and c), and a typical trajectory in AE or CE selected and demonstrated in b and d, respectively.

boundary jet likely separates these two eddies and made them independent from each other.

4.4 *Computational error and sensitivity test*

Sensitivity experiments, which are introduced in Table 2, were employed to estimate and discuss the computational error.

4.4.1 *Time step and integration period*

In the 2D experiment, the computational error is always maintained at a very small value in the convergent flow (Fig. 10a), even when we use a time step as large as 600 s. In the divergent flow, however, the maximum computational error is much larger (Fig. 10b), and few flows have a computational error as large as 200 km after 1 440 hours of integration. In the 3D experiments, the computational errors grew very slowly in the CE (Assum Exp7, Fig. 10c). When the particles moved in the eddy with an integration period of less than 1 000 hours, the computational error was always maintained below 5 km. Actually, 85% of the particles can always maintain computational errors smaller than 5 km in the 1 440-hour integration when the time step is no more than 60 s (not given). In the AE (Assum Exp8, Fig. 10d), the results are nearly the same. When the time step is smaller than 60 s, the maximum computational error in all particles could be maintained smaller than 25 km over a long integral period (i.e., 2 months). Moreover, more than 85% of particles could maintain computational errors smaller than 5 km. However, when the time step was larger than 300 s, the computational error grew fast and reached values as high as 300 km during the 1 440 h integration.

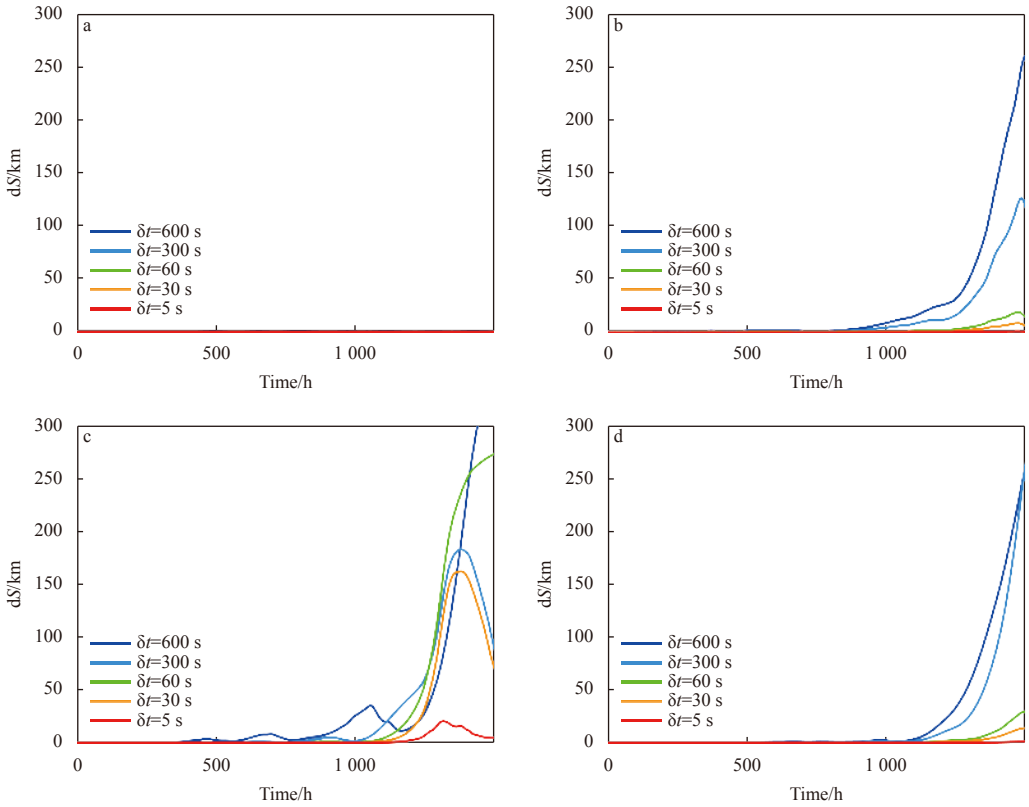

Fig. 10. Maximum computational error (a and b) estimated from particles in the CE and AE in Exp6 and Assum Exp6, respectively. The maximum computational error (c) estimated from particles in Assum Exp7, and the maximum computational (d) estimated from particles in Assum Exp8. The blue, cyan, green, orange, and red lines indicate the correlation coefficient obtained using the time steps of 600 s, 300 s, 60 s, 30 s and 5 s, respectively.

Compared with the computational errors in the idealized simulation and the realistic simulation, we found that the computational error is much smaller in the realistic simulation during the same integral period of the Lagrangian analysis. The main reason for the smaller computational errors in the realistic simulation analysis than in the idealized simulation analysis is because of the different horizontal resolution. The horizontal resolution of the realistic simulation is five times of that of the idealized simulation. As a result, we suggest that the period of the Lagrangian analysis, which was applied to a 5 km-resolution dataset, could be more than 2 months, whereas we chose a time step smaller than 60 s for the Lagrangian analysis.

4.4.2 *Current features*

We also estimate how current features influence the computational error when the Lagragian analysis is applied to a realistic simulation. In general, the correlation coefficient between the current feature and the growth rate of the computation error increased (Fig. 11) with a larger time step, which is consistent with the conclusion in the idealized simulation. In the downwelling, the correlation coefficient between the divergence (Fig. 11a; vertical velocity shear, Fig. 11b) and the growth rate of the computation error was larger than 0.025 (0.05), and the sign was consistent with the results in the idealized simulation. However, the correlation coefficient between the vertical vorticity and the growth rate of the computation error (Fig. 11c) was 0.01 and the sign was opposite the result in the idealized simulation; thus, we think that the relationship between the vertical vorticity and the growth rate of the computational error was not significant. In the upwelling, the correlation coefficient between the divergence (Fig. 11d; vertical velocity shear, Fig. 11e) and the growth rate of the computation error was more than 0.11 (0.08), which is consistent with the conclusions drawn in the idealized simulation. The correlation coefficient between the vertical vorticity and the growth rate of the computational error (Fig. 11f) was only –0.04. The results are consistent with our previous conclusions.

The reason that the correlation coefficient is smaller in the realistic simulation is that the sample number is four times larger than that in the idealized eddy. However, the opposite sign in the vertical vorticity analysis indicates that it should be eliminated from our consideration. Based on the results from the idealized simulation and realistic simulation, we found that the growth rate of the computational error is mainly determined by the divergence and vertical velocity shear, which means that the computational error is more likely to increase under a more divergent and stronger vertical diffusive flow.

5 Results and analysis

In this study, we analyzed an idealized mesoscale eddy and performed a realistic simulation of the AE/CE eddy pair off the central Vietnam. In the idealized simulation, a mesoscale eddy was trapped over a seamount and downwelling (upwelling) appeared over (along) the seamount. The downwelling (upwelling) induced positive (negative) vorticity over (along) the seamount, which drove the current to rotate cyclonically (anticyclonically). In the AE/CE eddy pair, downwelling/upwelling appeared inside the anticyclonic/cyclonic eddy since the convergence/divergence appeared at the surface and divergence/convergence ap-

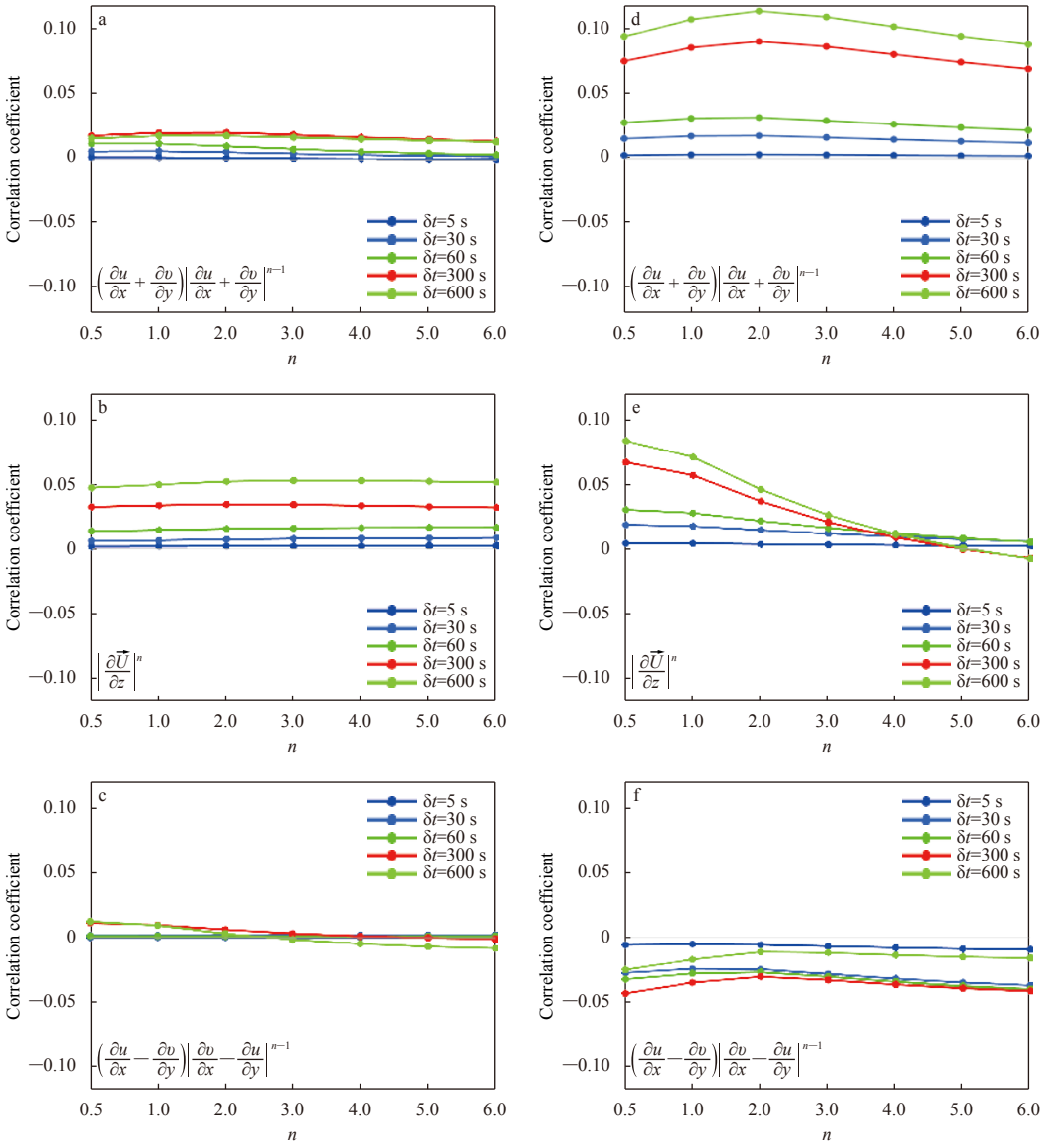

Fig. 11. Same as Fig.6 but the current speed is neglected. a, b, c. Correlations coefficient estimated from Assum Exp7; and d, e, f. correlation coefficients estimated from Assum Exp8. The blue, cyan, green, orange, and red lines indicate the correlation coefficient obtained using the time steps of 600 s, 300 s, 60 s, 30 s and 5 s, respectively.

peared in the lower layers. However, by applying the Lagrangian analysis to the realistic eddy-pair, we suggested the readers to be more careful, when select the position to put the tracers. As in the real ocean, the vertical motion is not homogenous inside the eddy, or even be in the opposite direction. Careless selection may lead to wrong eddy structure demonstration.

Compared with previous studies, we described the eddy structure to a greater extent using a Lagrangian view in several ways.

In the Lagrangian analysis of the idealized mesoscale eddy, the horizontal current was first demonstrated at the surface and lower layers. The distribution of the particles, with their colors varying over time along the trajectories, demonstrated how the current converged to the center of the eddy at the surface and converged to the upwelling zone in the bottom layer. The convergence at the surface caused the particles to eventually accumulate in a small zone. Thus, the computational error always approached zero in long-term integrations. On the other hand, the computational error was always larger in the bottom layer because the particles diverged rapidly due to the current distribution. In the realistic simulation, the particles converged (diverged) in the upper layer of the AE (CE) and diverged (converged) in the lower layer of the AE (CE). The computational error is always larger in the divergent flow than in the convergent flow, which is consistent with the results of the idealized simulation.

The most important part of this study is that the 3D structure of the mesoscale eddy was well demonstrated via the Lagrangian analysis. In the idealized mesoscale eddy, we released particles at the surface and tracked their trajectories in the following integration. The particles of different colors in different periods suggested that the current rotated and converged in the horizontal panel and sunk down to lower layers inside the mesoscale eddy. The particles stayed inside the eddy until they reached the bottom and sunk along the seamount to lower layers. We also released particles in lower layers outside the mesoscale eddies. The

particles with different colors in different periods suggested that the water in the lower layer compensated for the water being sucked into the eddy via upwelling. However, the results suggested that only the water in the upwelling zone at the bottom layer could move upward and return to the surface. In the dipole pattern, we released the particles in the upper (lower) layer of the AE (CE). The particles converged to the center of the eddy due to the convergent flow; meanwhile, the particles sank (rose) to lower (upper) layers due to the downwelling (upwelling) inside the AE (CE). The particles of different colors in different periods suggested that the vertical motion inside the eddy pair is not horizontally uniform.

In our realistic simulation, we also found that fluid exchange does not occur between the AE and CE and the AE/CE pairs are isolated by the northeastward jet between them. As a result, the particles cannot move from the CE to AE and vice versa. Actually, when the particles moved out of the eddies, they would move northeastward carried by the boundary jet along the coast of Vietnam.

We cannot compare the computational errors for the results with different resolutions since we do not have an actual "real value". However, 85% of particles could maintain a computational error below 3 km in the 3D experiments (1 km in the idealized experiments) if we employed a time step of no more than 60 s and even we integrated the information over 1 440 h (60 d). If the time step is no more than 60 s and the integral period is shorter than 500 h, all the particles can maintain computational errors at an acceptable value (i.e., 1 km). However, when the time step is larger than 300 s, the computational error grows significantly in a short period, which indicates that the trajectories are unconvincing.

Further analysis suggested that the growth rate of the computational error was related to divergence and vertical velocity shear. As the divergence (vertical velocity shear) increased, the computational error increased. This relationship was more significant with larger time steps. However, the growth rate of the computational error was not as sensitive to the current speed or vertical vorticity in this study.

The purpose of the study was to demonstrate the 3D structure of the mesoscale eddy from a Lagrangian perspective, and we employed both an idealized simulation and a realistic simulation. To simplify this analysis, we assumed that the eddy was constant, which is unlikely to be realistic. However, we focused on the Lagrangian trajectories and computational error growth rate, which were both well presented in this study. Additionally, we demonstrated the relative independence of Vietnam dipoles via the Lagrangian analysis.

Because the Lagrangian analysis could adequately describe the structures of the mesoscale eddies, which typically have greater speeds and larger variations than usual currents, we could confidently use the Lagrangian analysis to simulate the trajectories of the particles in a predicted current with a suitable time step and total integral period. The use of this Lagrangian calculation tool in mesoscale current simulations will be studied further in our future work.

Acknowledgements

We are grateful to Haijun Yang for providing valuable suggestions.

References

Adams K A, Hosegood P, Taylor J R, et al. 2017. Frontal circulation and submesoscale variability during the formation of a southern ocean mesoscale eddy. Journal of Physical Oceanography, 47(7): 1737–1753, doi: 10.1175/JPO-D-16-0266.1

Chu Xiaoqing, Xue Huijie, Qi Yiquan, et al. 2014. An exceptional anticyclonic eddy in the South China Sea in 2010. Journal of Geophysical Research: Oceans, 119(2): 881–896, doi: 10.1002/2013JC009314

Dai Haijin, Cui Jian, Yu Jingping. 2017. Revisiting mesoscale eddy genesis mechanism of nonlinear advection in a marginal ice zone. Acta Oceanologica Sinica, 36(11): 14–20, doi: 10.1007/s13131-017-1134-8

Dong Changming, Lin Xiayan, Liu Yu, et al. 2012. Three-dimensional oceanic eddy analysis in the Southern California Bight from a numerical product. Journal of Geophysical Research: Oceans, 117(C7): C00H14

Döös K, Nycander J, Coward A C. 2008. Lagrangian decomposition of the Deacon Cell. Journal of Geophysical Research: Oceans, 113(C7): C07028

Fang Wendong, Fang Guohong, Shi Ping, et al. 2002. Seasonal structures of upper layer circulation in the southern South China Sea from in situ observations. Journal of Geophysical Research: Oceans, 107(C11): 3202

Gula J, Molemaker M J, McWilliams J C. 2015. Topographic vorticity generation, submesoscale instability and vortex street formation in the Gulf Stream. Geophysical Research Letters, 42(10): 4054–4062, doi: 10.1002/2015GL063731

Gula J, Molemaker M J, McWilliams J C. 2016. Topographic generation of submesoscale centrifugal instability and energy dissipation. Nature Communications, 7: 12811, doi: 10.1038/ncomms12811

Häkkinen S. 1986. Coupled ice-ocean dynamics in the marginal ice zones: Upwelling/downwelling and eddy generation. Journal of Geophysical Research: Oceans, 91(C1): 819–832, doi: 10.1029/JC091iC01p00819

Johannessen J A, Johannessen O M, Svendsen E, et al. 1987. Mesoscale eddies in the Fram Strait marginal ice zone during the 1983 and 1984 Marginal Ice Zone Experiments. Journal of Geophysical Research: Oceans, 92(C7): 6754–6772, doi: 10.1029/JC092iC07p06754

Kjellsson J, Döös K. 2012. Lagrangian decomposition of the Hadley and Ferrel cells. Geophysical Research Letters, 39(15): L15807

Kuo N J, Zheng Quanan, Ho C R. 2000. Satellite observation of upwelling along the western coast of the South China Sea. Remote Sensing of Environment, 74(3): 463–470, doi: 10.1016/S0034-4257(00)00138-3

Lemarié F, Kurian J, Shchepetkin A F, et al. 2012. Are there inescapable issues prohibiting the use of terrain-following coordinates in climate models?. Ocean Modelling, 42: 57–79, doi: 10.1016/j.ocemod.2011.11.007

Lin Xiayan, Dong Changming, Chen Dake. 2018. Cross-basin particle transport by a warm eddy southwest of Taiwan Island. Journal of Tropical Oceanography (in Chinese), 37(3): 9–18

Liu A K, Häkkinen S, Peng C Y. 1993. Wave effects on ocean-ice interaction in the marginal ice zone. Journal of Geophysical Research: Oceans, 98(C6): 10025–10036, doi: 10.1029/93JC00653

Manucharyan G E, Timmermans M L. 2013. Generation and separation of mesoscale eddies from surface ocean fronts. Journal of Physical Oceanography, 43(12): 2545–2562, doi: 10.1175/JPO-D-13-094.1

Manucharyan G E, Thompson A F. 2017. Submesoscale sea ice-ocean interactions in Marginal Ice Zones. Journal of Geophysical Research: Oceans, 122(12): 9455–9475, doi: 10.1002/2017JC012895

McWilliams J C. 2016. Submesoscale currents in the ocean. Proceedings of the Royal Society A: Mathematical, Physical and Engineering Sciences, 472(2189): 20160117, doi: 10.1098/rspa.2016.0117

Moore A M, Arango H G, Broquet G, et al. 2011. The Regional Ocean Modeling System (ROMS) 4-dimensional variational data assimilation systems: Part Ⅲ-Observation impact and observation sensitivity in the California Current System. Progress in Oceanography, 91(1): 74–94, doi: 10.1016/j.pocean.2011.05.005

Nakamura T, Matthews J P, Awaji T, et al. 2012. Submesoscale eddies

near the Kuril Straits: Asymmetric generation of clockwise and counterclockwise eddies by barotropic tidal flow. Journal of Geophysical Research: Oceans, 117(C12): C12014

Nencioli Francesco, Dong Changming, Dickey Tommy, et al. 2010. A Vector Geometry-Based Eddy Detection Algorithm and Its Application to a High-Resolution Numerical Model Product and High-Frequency Radar Surface Velocities in the Southern California Bight. Journal of Atmospheric and Oceanic Technology, 27(3): 564–579, doi: 10.1175/2009JTECHO725.1

Okubo A. 1970. Horizontal dispersion of floatable particles in the vicinity of velocity singularities such as convergences. Deep Sea Research and Oceanographic Abstracts, 17(3): 445–454, doi: 10.1016/0011-7471(70)90059-8

Shchepetkin A F, McWilliams J C. 2005. The Regional Oceanic Modeling System (ROMS): A split-explicit, free-surface, topography-following-coordinate oceanic model. Ocean Modelling, 9(4): 347–404, doi: 10.1016/j.ocemod.2004.08.002

Torres T S, Klein P, Menemenlis D, et al. 2018. Partitioning ocean motions into balanced motions and internal gravity waves: a modeling study in anticipation of future Space missions. Journal of Geophysical Research: Oceans, 123(11): 8084–8105, doi: 10.1029/2018JC014438

van Sebille E, Griffies S M, Abernathey R, et al. 2018. Lagrangian ocean analysis: Fundamentals and practices. Ocean Modelling, 121: 49–75, doi: 10.1016/j.ocemod.2017.11.008

Wang Guihua, Chen Dake, Su Jilan. 2006. Generation and life cycle of the dipole in the South China Sea summer circulation. Journal of Geophysical Research: Oceans, 111(C6): C06002

Weiss J. 1991. The dynamics of enstrophy transfer in two-dimensional hydrodynamics. Physica D: Nonlinear Phenomena, 48(2–3): 273–294, doi: 10.1016/0167-2789(91)90088-Q

Xie Shangping, Xie Qiang, Wang Dongxiao, et al. 2003. Summer upwelling in the South China Sea and its role in regional climate variations. Journal of Geophysical Research: Oceans, 108(C8): 3261, doi: 10.1029/2003JC001867

Zhang Xueyan, Dai Haijin, Zhao Jun, et al. 2019. Generation mechanism of an observed submesoscale eddy in the Chukchi Sea. Deep Sea Research Part I: Oceanographic Research Papers, 148: 80–87, doi: 10.1016/j.dsr.2019.04.015

Appendix A: Mesoscale eddy simulation and analysis

Previous studies suggested there are three mesoscale eddy genesis mechanisms generally. The first one is the topography variations in the bottom, which increases the vorticity and form mesoscale eddies via potential vorticity conservation (Gula et al., 2015, 2016). The second one is unstable energy induced by barotropic and/or baroclinic instability can help small scale turbulence grow into mesoscale eddies (Nakamura et al., 2012; Manucharyan and Timmermans, 2013; Manucharyan and Thompson, 2017). The third eddy genesis mechanism is in the ice zone, as the momentum transferred from the wind is more efficiently via sea ice than to the ocean directly, there is velocity shear at the ice boundary, which can be increased and form mesoscale eddies by nonlinear advection of the current (Häkkinen, 1986; Liu et al., 1993; Dai et al., 2017).

A mesoscale eddy generated by the first mechanism can be maintained in the same region. Mesoscale eddies generated by the second mechanism form quickly but always move following the jet or the front. A great number of the eddies are produced at the same time and can hardly be separated from each other. Mesoscale eddies produced by the third eddy genesis mechanism are generally very weak, especially in deep water. As a result, we employ the second mechanism to generate mesoscale eddies with a numerical ocean model and use topography to maintain the eddy in the same region.

A1 Model and experiment settings

The numerical ocean model used in this study is the Regional Oceanic Modeling System (ROMS), which solves 3D hydrostatic primitive equations (Shchepetkin and McWilliams, 2005) with vertical hybrid z-sigma coordinates (Lemarié et al., 2012). The theoretical framework of this model is written as follows:

$$\frac{\partial \vec{u}}{\partial t} + \left(\vec{u} \cdot \nabla_{\perp}\right) \vec{u} + \vec{w}\frac{\partial \vec{u}}{\partial z} = -\nabla_{\perp}\Phi - f\vec{z} \times \vec{u} + \vec{\tau}_{\mathrm{aw}}, \tag{A1}$$

$$\frac{\partial \Phi}{\partial z} + \frac{g\rho_{\mathrm{w}}}{\rho_0} = -\frac{\partial \Gamma}{\partial z}, \tag{A2}$$

$$\nabla_{\perp} \cdot \vec{u} + \frac{\partial w}{\partial z} = 0, \tag{A3}$$

$$\frac{\partial c}{\partial t} + \left(\vec{u} \cdot \nabla_{\perp}\right) c + w\frac{\partial c}{\partial z} = D^c + Q^c, \tag{A4}$$

where $\vec{v} = (u, v)$ is the current velocity vector; u, v, and w are the current velocities in the x, y and z directions, respectively; and Φ is the sea surface potential function, and f is the Coriolis parameter. In this case, f=0.000 1 s^{-1}, addition, c is the tracer (i.e., temperature, salinity), D^c represents the tracer diffusion, Q^c is the source of the tracer. τ_{aw} is the wind stress exerted on the current, and ρw and ρ_0 are the water density and water reference density, respectively.

The model is configured on a 200 km×100 km domain with a horizontal resolution of 1 km. There are 40 grid levels in the vertical direction, spanning a total depth of 400 m. There, are north-south periodic boundaries and east-west periodic boundaries. In the model run, the reference water density is 1 027.5 kg/m^3. A front was located along the seamount in the initial field (Fig. A1a), and another two fronts appeared as ellipses close to the seamount (Fig. A1b). In addition, the initial velocity fields are set to zero. A constant and uniform wind (1.8 m/s, Fig. A1c, vectors) is applied to the entire domain, while a seamount is placed at the center of the modeled region, with a total height of 150 m and a topography gradient of 5 m/km (Fig. A1c, shading). The model is integrated for 3 model days, although the result at the end of the 6th hour is used for more beautiful eddy structure (We aim to introduce a better method of presenting the eddy structure instead of discussing the eddy evolution).

A2 Mesoscale eddy analysis

The fronts contained substantial amounts of available potential energy. However, they existed in an unstable state and slumped over a short time. After 6 hours of integration, the front over the seamount diminished significantly (Fig. A2a). Two fronts near the seamount diminished and were separated into a few segments (Fig. A2b). When the density over the seamount was larger than that of the surrounding water, downwelling occurred (Fig. A2c). Close to the seamount, lighter and denser water corresponded to upwelling and downwelling, respectively (Fig. A2c). When the fronts slumped due to gravity, the available potential energy was converted into a current, which helped the turbulence grow into a mesoscale eddy. The primary eddy grew over the seamount and was maintained over the seamount. The downwelling determined the positive vorticity over the seamount, and the current rotated cyclonically (Fig. A2d).

In a 3D structure, the downwelling over the seamount and the upwelling along the seamount dominated the entire column (Fig. A3a, b). On the eastern and western sides of the seamount, mixing occurred with upwelling and downwelling. Due to the distribution of upwelling and downwelling, a convergence formed at the bottom of the seamount (Fig. A3c, x=75 km and x=125 km) and a divergence formed at the bottom of the downwelling (Fig. A3c, x=50 km and x=150 km). Due to vertical convection, the relative vorticity was positive (negative) when there was downwelling (upwelling). Thus, du/dy is negative (positive) over (along) the seamount (Fig. A3d). In contrast, dv/dx is positive (negative) over (along) the seamount (Fig. A3e). The currents mainly flow over the seamount in the x direction, as v is small in the section x=100 km (Fig. A3f). Because baroclinic instability was dominant in this study, the potential vorticity conservation law was invalid.

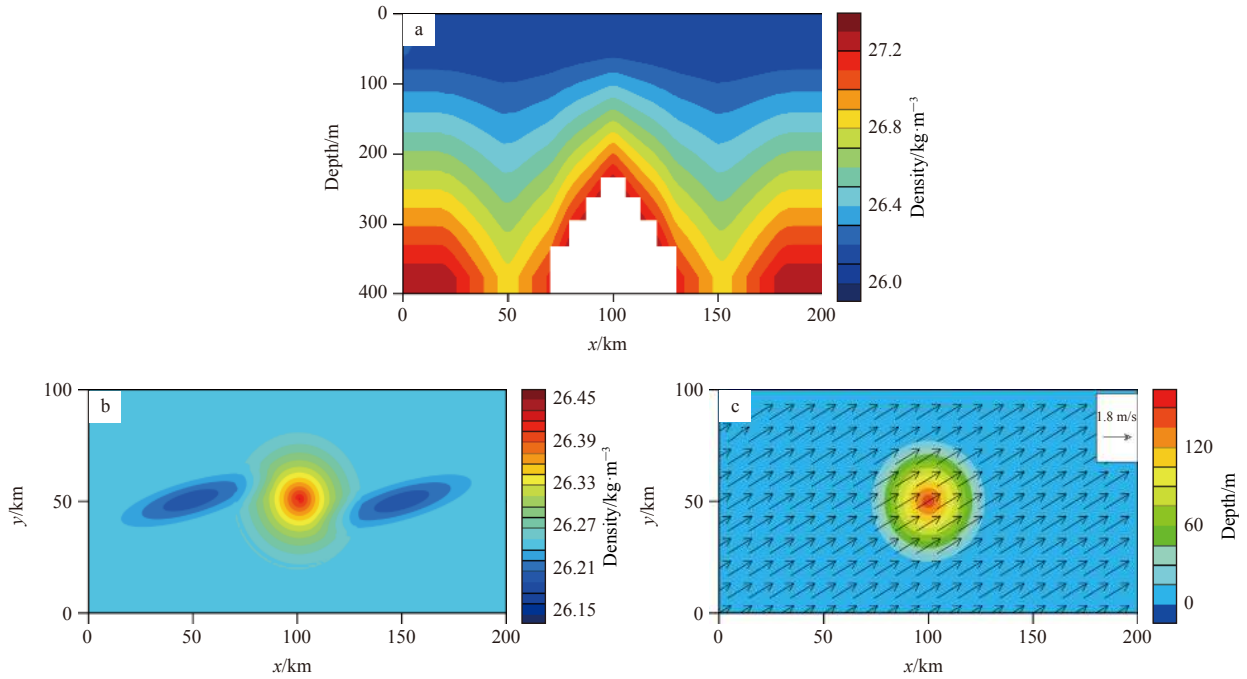

Fig. A1. Distribution of the initial density across the section of y=51 km (a) and at a depth of 160 m (b); and distributions of the bottom topography and the wind force (c).

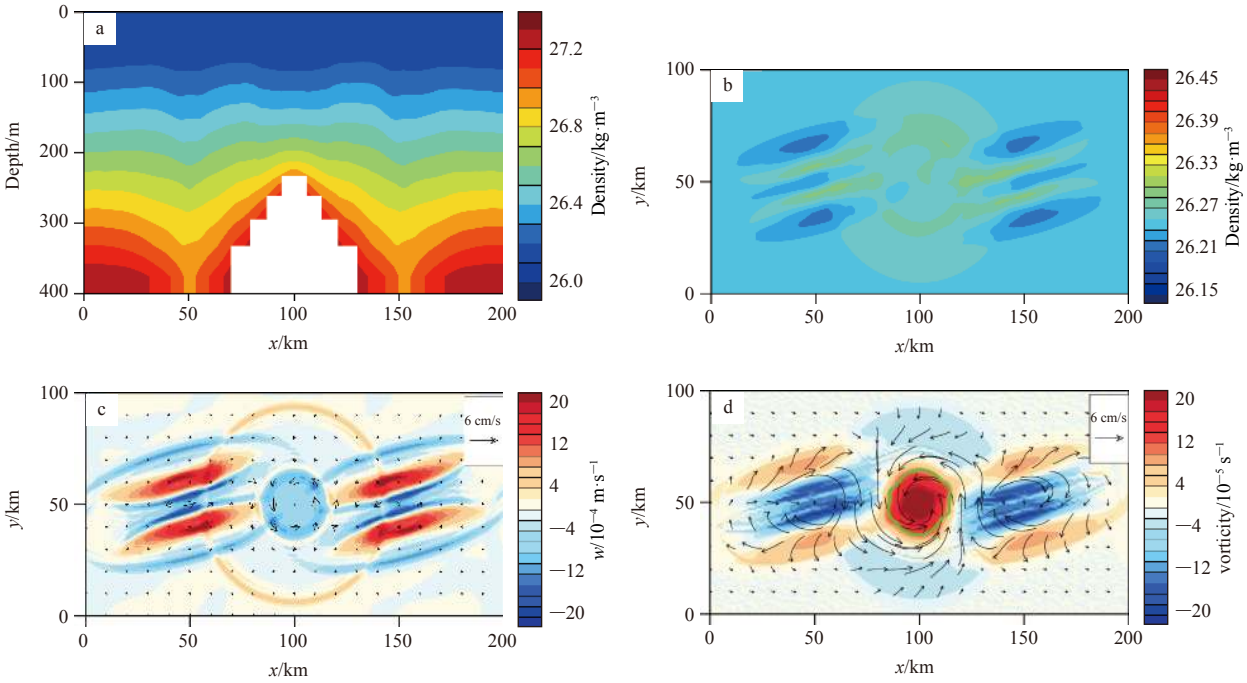

Fig. A2. Distribution of density across the section of y=51 km at the 6th hour (a), distribution of the initial density at a depth of 160 m at the 6th hour (b), distributions of the vertical averaged velocity in the horizontal and vertical directions (c), distributions of the surface current and vertical vorticity (d).

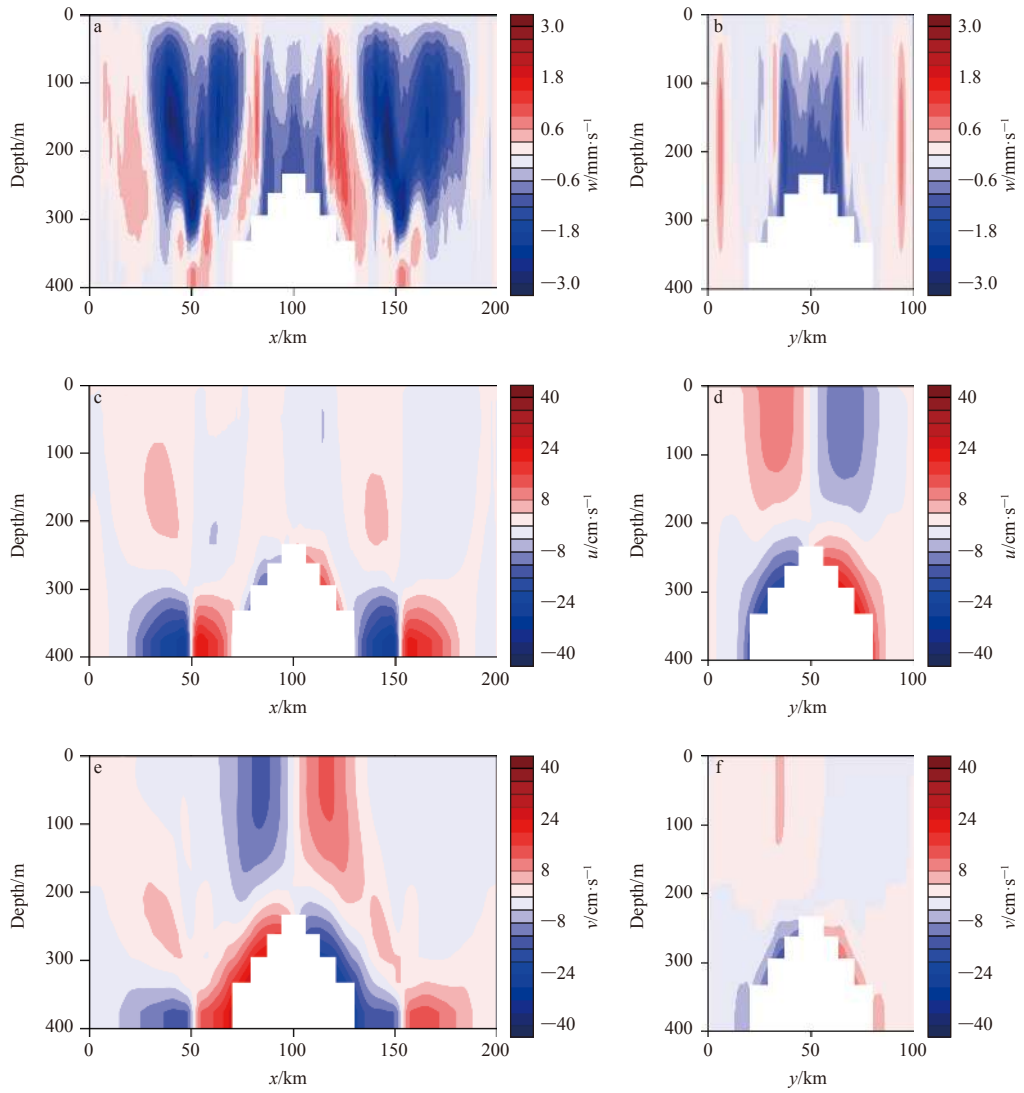

Fig. A3. Distributions of the current velocity across the section of y=50 km in the z, x, and y directions (a, c, and e), and across the section of x=100 km in the z, x, and y directions (b, d, and f).

Appendix B: Eddy pair in the South China Sea

B1 Experiment settings

The west part of the SCS (4°–18°N, 106°–116°E) was simulated by ROMS (University of Rochester version), with a resolution of (1/20°) in the horizontal direction and 48 levels in the vertical direction. To improve the accuracy of our simulation, a strong constraint 4D-Var (I4DVAR) scheme (Moore et al., 2011) was implemented into the ROMS to finish data assimilation with satellite observations (sea surface temperature (SST) and sea level anomaly (SLA)) and *in situ* temperature/salinity (T/S) profile (Argo, Conductivity-Temperature-Depth recorder (CTD), etc). The gridded bathymetric data from GEBCO08 (https://www.gebco.net/data_and_products/gridded_bathymetry_data/) with a minimum depth of 10 m and a maximum depth of 5 500 m were used for the topography. Three-hourly wind (ERA-Interim, https://www.ecmwf.int/en/forecasts/datasets/reanalysis-datasets/era-interim) from the European Centre for Medium-Range Weather Forecasts (ECMWF) was used as wind forcing. We employ open boundary condition in each boundary. At the boundary, the current was relaxed to a climate status, which is satisfied with monthly reanalysis data (The Simple Ocean Data Assimilation, SODA 3.3.1, https://www.atmos.umd.edu/~ocean/index_files/soda3.3.1_mn_download.htm). Along with model integration, satellite SST from the Advanced Very High-Resolution Radiometer (AVHRR, ftp://eclipse.ncdc.noaa.gov), SLA from the satellite derived Sea Surface Height above Geoid (AVISO, http://www.aviso.oceanobs.com/duacs/), in situ T/S profile data from EN4.2.1 (http://hadobs.metoffice.com/en4/download.html) were assimilated and input into the ocean model every 4 d. The model was integrated for 9 months, which started on January 1, 2013, while we employed the results from September 2013.

B2 Three-dimensional structure of the eddy pair

In our simulation, the dipole structure of the eddy pair appeared off the central Vietnam during September, 2013 (Fig. B1a), which is consistent with the observations (Fig. B1b). We also employ a trajectory of Argo No. 5 904 191 (Fig. B1c, green line) at the layer of –1 200 m through the whole September. The eddy captured by the Argo can also be found in our simulation (Fig. B1c, vector), although the Argo located more to the west, because of the large horizontal decorrelation scale used in the assimilation setting. Back to the current field, several eddies (not given) were observed with the eddy boundary definition. However, in this simulation, the boundary defined with vector geometry method (Nencioli et al., 2010) proposed by Dong et al., (2012) can better capture the eddy features than the OW method. The results suggested that only the primary AE/CE pair always stays in the region of (8°–15°N, 109°–114°E) through the whole of September 2013.

The outline of the AE/CE pair (Fig. B2) suggested that the radius of the AE (Fig. B2a, red line) expanded to as much as 131 km (average radius is 116 km), which is larger than the radius of the CE (110 km and 88 km for the maximum and average radius, respectively, Fig. B2a, blue line), because the positive potential vorticity increased when the flow climbed over the seamounts by the potential vorticity conservation law. However, the CE (Fig. B2b blue line) extended to deeper layers (1 000 m) than the AE (350 m). The AE/CE pair on September 13, 2013 was chosen for better analysis since the eddies appeared as quasi-cylinders, which made the analysis simpler.

In the profile (x=113°E, Fig. B3a), eastward flow occurred in the south (north) part of the CE(AE), while westward flow (Fig. B3b) occurred in the north (south) part of the CE (AE), which indicated that the current rotated cyclonically (anticyclonically) in the CE (AE). The zonal flow, which has a maximum velocity as high as 1.4 m/s, was nearly uniform in each layer above 350 m, as a result, downwelling (upwelling, Fig. B3c) occurred in the AE (CE), although the vertical motion was not consistent inside the eddies. Disturbed by the vertical flow, the isotherms (Fig. B3d) sank (lifted) in the AE (CE).

The profile of the eddies were separately checked (Figs B4a, b). As the current rotated anticyclonically in the AE, northward and southward flows occurred in the west and east part of AE (Fig. B4c), whereas southward and northward flows occurred in the west and east part of CE (Fig. B4d). For the vertical motion, the results were consistent with the meridional profile. There was approximately uniform downwelling (Fig. B4e, upwelling, Fig. B4f) inside the AE (CE), although the downwelling inside the AE is more evident on September 11, 2013 (not given).

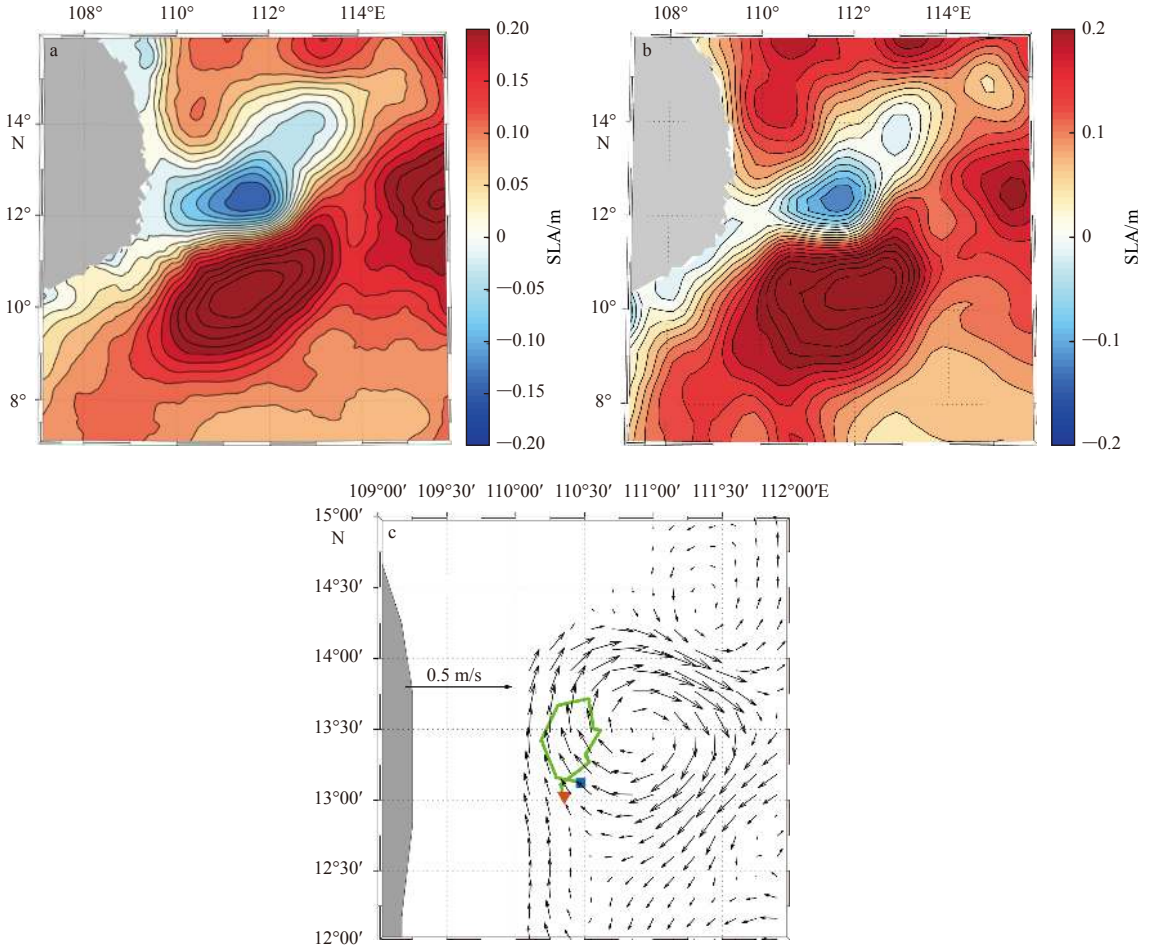

Fig. B1. Distribution of the SLA in our simulation (a) and the AVISO (b) on September 13, 2013, and the trajectory of Argo No. 5904191 (green line) through the whole September, 2013 and the current field at the layer of –1 200 m (vector) on September 13, 2013 (c).

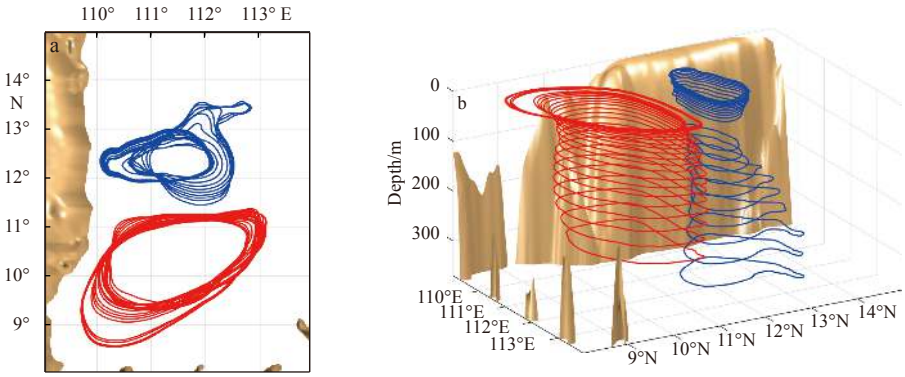

Fig. B2. Vertical view of the eddy boundary of AE (red line) and CE (blue line) in each layer (a), and 3D structure of the eddy boundary (b). The orange shading indicates the topography.

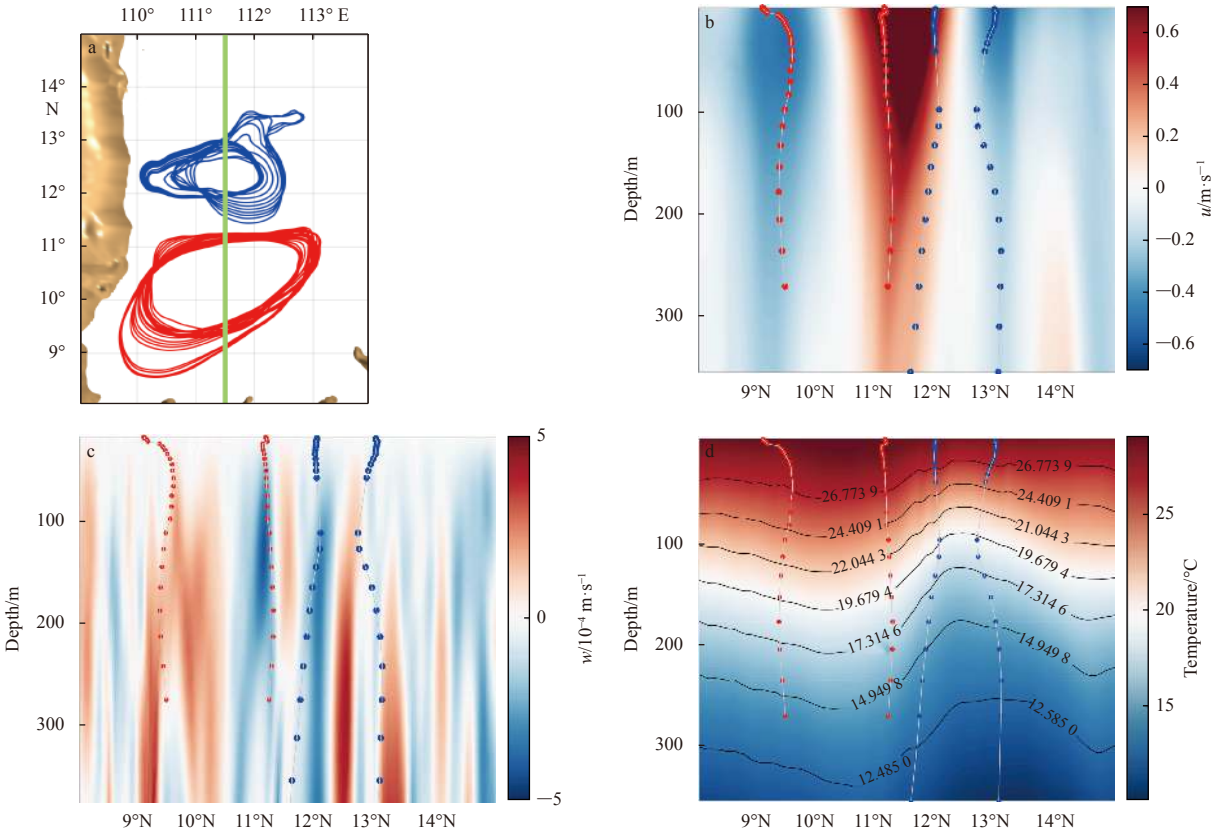

Fig. B3. Vertical view of the eddy boundary of AE (red line) and CE (blue line) in each layer (a) with a green line nearly across the centers of the two eddies; the vertical profile of the velocity in the zonal and vertical direction. (b and c) along the green line in a; The red and blue dot lines presented the eddy boundary in each layer and the vertical profile of temperature and selected isotherms (d).

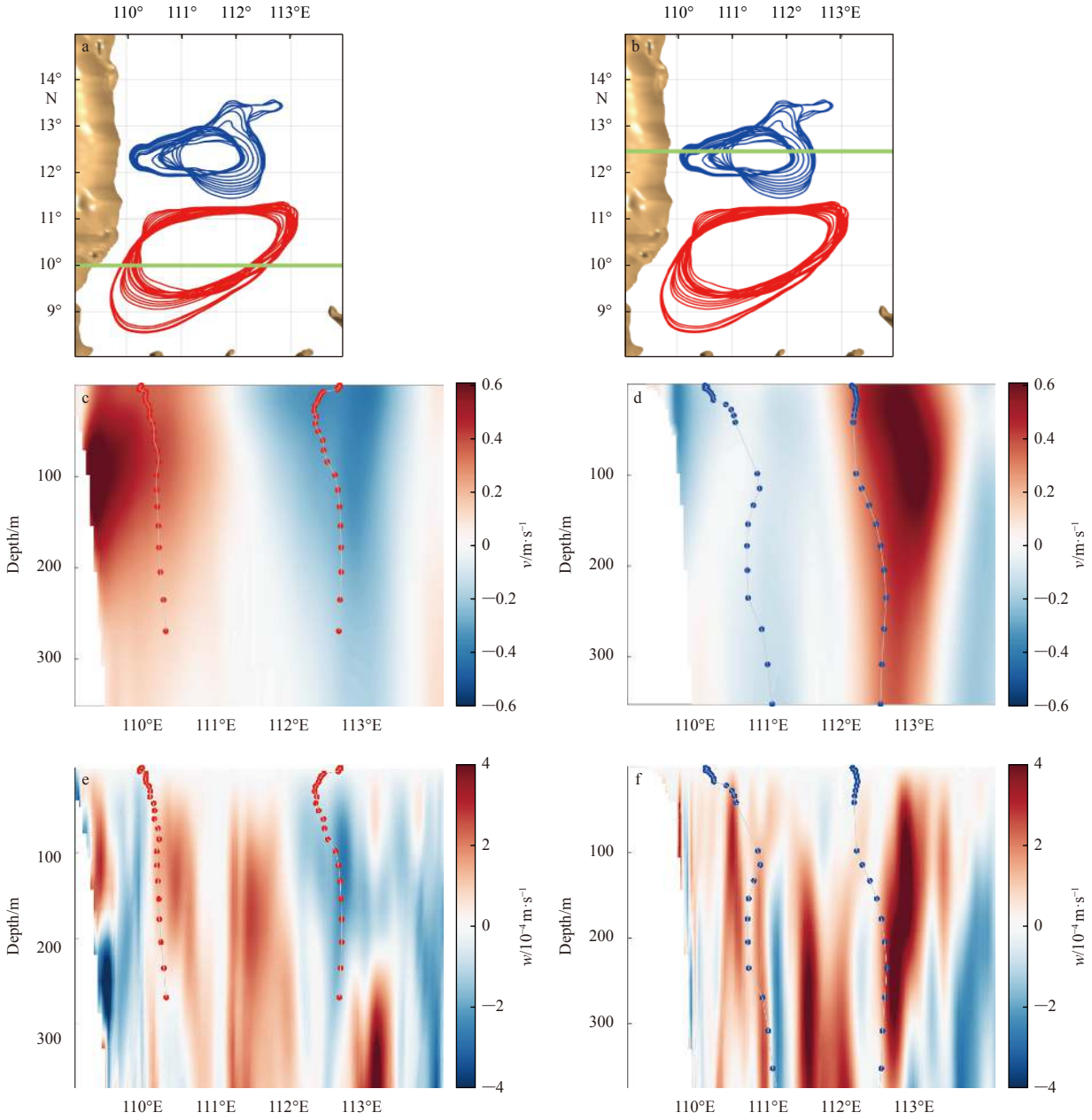

Fig. B4. Vertical view of the eddy boundary of AE (red line) and CE (blue line) ineach layer are shown in a and b, green line indicates the slice we choosein the AE (a) and CE (b). Along the green line in a and b, the vertical profileof the velocity in the meridional (unit: m/s) and vertical direction (unit:0.1mm/s) are shown as shading in c, d, e and f, respectively, while the red and blue dot lines presented the eddy boundary in each layer.